Nanoscale optical tomography with cathodoluminescence spectroscopy

Ashwin C. Atre[1]*, Benjamin J. M. Brenny[2], Toon Coenen[2], Aitzol García-Etxarri[1], Albert Polman[2] and Jennifer A. Dionne[1]

Tomography has enabled the characterization of the Earth's interior, visualization of the inner workings of the human brain, and three-dimensional reconstruction of matter at the atomic scale. However, tomographic techniques that rely on optical excitation or detection are generally limited in their resolution by diffraction. Here, we introduce a tomographic technique—cathodoluminescence spectroscopic tomography—to probe optical properties in three dimensions with nanometre-scale spatial and spectral resolution. We first obtain two-dimensional cathodoluminescence maps of a three-dimensional nanostructure at various orientations. We then use the method of filtered back-projection to reconstruct the cathodoluminescence intensity at each wavelength. The resulting tomograms allow us to locate regions of efficient cathodoluminescence in three dimensions across visible and near-infrared wavelengths, with contributions from material luminescence and radiative decay of electromagnetic eigenmodes. The experimental signal can be further correlated with the radiative local density of optical states in particular regions of the reconstruction. We demonstrate how cathodoluminescence tomography can be used to achieve nanoscale three-dimensional visualization of light–matter interactions by reconstructing a three-dimensional metal–dielectric nanoresonator.

Q1

Tomography enables the determination of a three-dimensional function from two-dimensional data. Originally driven by the need for a non-invasive technique to peer inside the human body, the development and application of tomography has had a significant impact on a wide range of disciplines, from medical diagnosis[1] to oceanography[2] and seismology[3]. While conventional tomographic techniques yield three-dimensional structural or chemical information with macroscopic resolution, recent advances in electron microscopy have enabled nanoscale reconstruction of material geometries[4–7]. Notably, electron tomography has been used to reconstruct nanoparticles with atomic-scale resolution[8,9] and to identify their different chemical constituents in three dimensions[10–13].

However, optical tomography with subwavelength, nanometre-scale resolution remains a significant challenge. For example, although super-resolution techniques can yield three-dimensional maps of molecular structure[14,15], they rely on fluorescent tagging and cannot probe the intrinsic radiative optical properties of the nanostructure. Nearly all other label-free techniques for probing nanoscale light–matter interactions are inherently two-dimensional. For example, scanning a physical probe such as a nanoscale tip[16–19] or fluorescent emitter[20–24] over an object creates a planar map of the optical modes or local density of optical states (LDOS). Similarly, a focused electron beam can act as a spatially localized but optically broadband impulse excitation on an object[25–30], but has historically been used to probe electromagnetic modes in two dimensions. Capturing the often complex three-dimensional nature of light–matter interactions with nanometre-scale spatial and spectral resolution remains a significant challenge.

Recently, the first label-free three-dimensional maps of nanoscale optical modes were obtained by combining two-dimensional electron-energy loss spectroscopy (EELS) with tomographic reconstruction methods[31,32]. In this Article, we introduce a complementary technique for the nanoscale interrogation of optical properties in three dimensions: cathodoluminescence tomography. Both EELS and cathodoluminescence rely on electron-beam excitation of a sample, but they are fundamentally distinct in terms of their detection mechanisms and signal interpretation. First, cathodoluminescence spectroscopy detects light emitted by a sample rather than the energy lost by electrons transmitted through the sample. This optical detection scheme currently allows higher spectral resolution than is afforded by EELS. Second, cathodoluminescence selectively detects radiative optical processes, whereas EELS indiscriminately probes both radiative and non-radiative processes. Therefore, unlike EELS, cathodoluminescence enables direct visualization of the material luminescence and radiative decay of electromagnetic modes. Together, the high spectral resolution and selective detection of radiative processes of cathodoluminescence tomography could elucidate, for example, the regions of highest radiative rate enhancement near a nanostructure or the distribution of radiative recombination sites in a semiconductor.

To demonstrate this new tomographic technique we first obtained a series of cathodoluminescence maps of a three-dimensional metal–dielectric nanostructure in various orientations. The method of filtered back-projection was then used to reconstruct the cathodoluminescence intensity, which we correlated with both the material luminescence and radiative LDOS. Owing to the high spatial and spectral resolution afforded by cathodoluminescence, this reconstruction provides detailed, three-dimensional spectral maps of radiative optical properties across the visible and near-infrared wavelengths.

Cathodoluminescence spectroscopy and two-dimensional imaging

Q2

As an example of cathodoluminescence spectroscopic tomography we consider a three-dimensional metal–dielectric crescent, or nanocup, as shown schematically in Fig. 1a. This is composed of a sub-wavelength dielectric core coated with a tapered metallic shell.

[1]Department of Materials Science and Engineering, Stanford University, Stanford, California 94305, USA. [2]Center for Nanophotonics, FOM Institute AMOLF, Science Park 104, Amsterdam 1098 XG, The Netherlands. *e-mail: aatre@stanford.edu

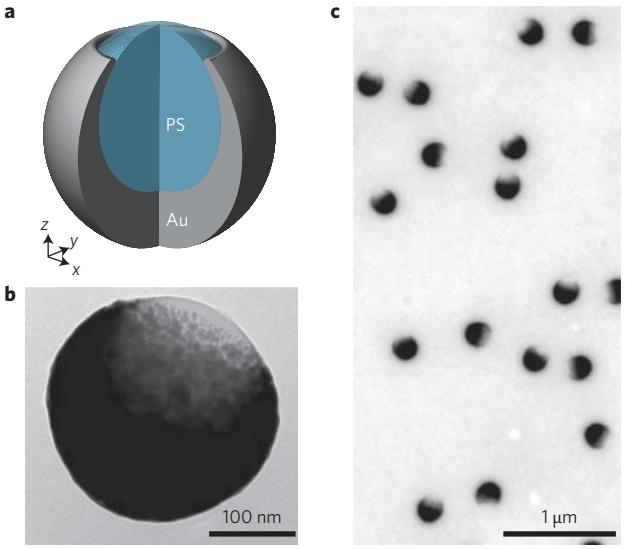

Figure 1 | Metal–dielectric crescents. a, Schematic of a crescent consisting of a polystyrene (PS) core (blue) and a Au shell (grey). **b**, Bright-field TEM image of an individual crescent. **c**, Wide-field TEM image of crescents.

This structure is well known for its abilities to harvest light over a large bandwidth[33–35], confine light on the nanoscale[36–40], support electric and magnetic modes[41,42] and serve as the constituent of an extremely broadband negative-index metamaterial at optical frequencies[43]. The plasmonic nanocrescent derives many of its interesting optical properties from the asymmetry of its core–shell geometry. The tapered metallic shell yields a broadband optical response, while the metallic discontinuity across the tips enables strong electric and magnetic resonances and field enhancements. However, the rotational symmetry of the crescent imparts it with a degree of insensitivity to polarization as well as relatively facile fabrication. Additionally, the complex three-dimensional structure of the crescent provides a powerful platform for demonstrating the potential of cathodoluminescence tomography.

The nanocrescents were fabricated by evaporating Au onto polystyrene spheres. Bright-field transmission electron microscopy (TEM) images of these Au–polystyrene crescents are shown in Fig. 1b,c. The figures reveal the axial symmetry of individual crescents, as well as their high degree of uniformity.

Cathodoluminescence spectroscopy was performed in a scanning electron microscope (SEM)[29,30]. Figure 2 presents cathodoluminescence measurements of crescents with different orientations, where θ is the angle between the axis of symmetry of the crescent (the z axis) and the incident beam direction. Note that this coordinate system co-rotates with the crescent such that the z axis is always aligned with the axis of symmetry; this axis of rotation is defined as the y axis. An angle of 0° corresponds to a crescent with tips pointing towards the substrate. Figure 2b shows the result of scanning the electron beam across the centre of a crescent oriented at an angle of 90°. As the electron beam passes through the tips of the crescent (darker lines), the cathodoluminescence signal peaks at a wavelength of ~850 nm. This lowest-energy resonance of the crescent is characterized by strong electric field enhancement near the sharp tips of the structure[36,40], as confirmed by finite-difference time-domain (FDTD) simulations (Fig. 2c and Supplementary

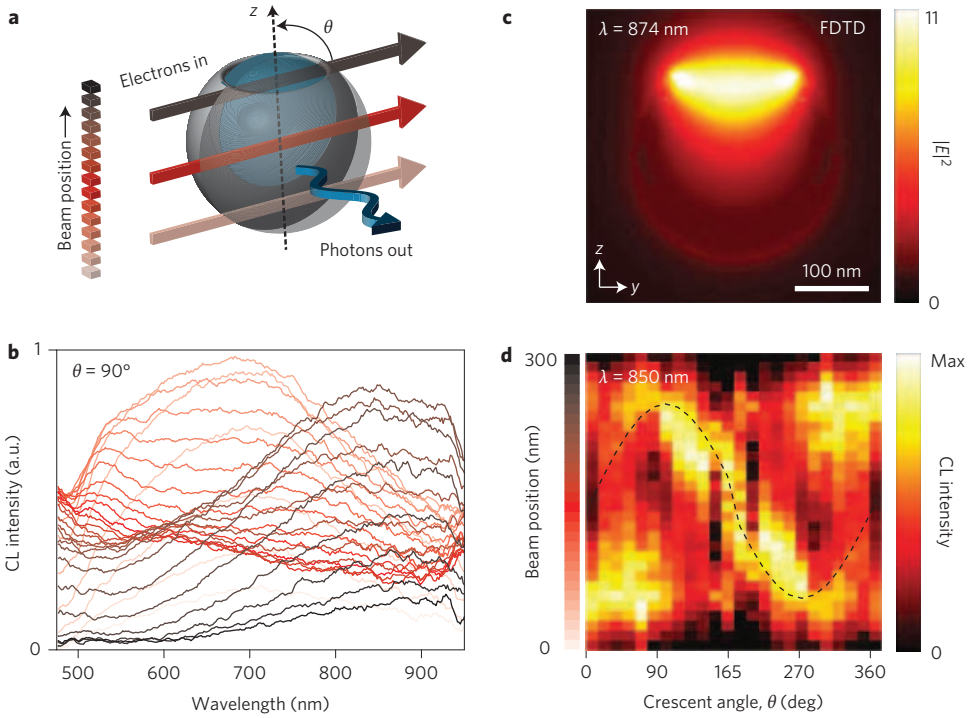

Figure 2 | Cathodoluminescence line scans. a, Schematic of the cathodoluminescence (CL) line scan, with the beam passing through the central z axis of the crescent (θ is the angle between the crescent's axis of symmetry and the electron beam). **b**, Experimental cathodoluminescence line scan of a crescent oriented at 90°, with darker colours corresponding to higher beam positions, as indicated in **a**. **c**, Cross-section of the scattered electric field intensity calculated by FDTD simulations for excitation with an x-polarized plane wave propagating in the $-z$ direction at a wavelength of 874 nm (the peak in the extinction efficiency). **d**, Experimental sinogram of normalized cathodoluminescence intensity line scans at a wavelength of 850 nm for crescents at various angles, where the vertical axis corresponds to the excitation positions shown schematically in **a**. Due to the reflection symmetry of the crescent, data from 0° to 165° are flipped and repeated for angles of 195° to 360°. A crescent at 180° was not available. The dashed-line overlay denotes the physical position of the centre of the gap between the tips of the crescent, derived from the crescent model.

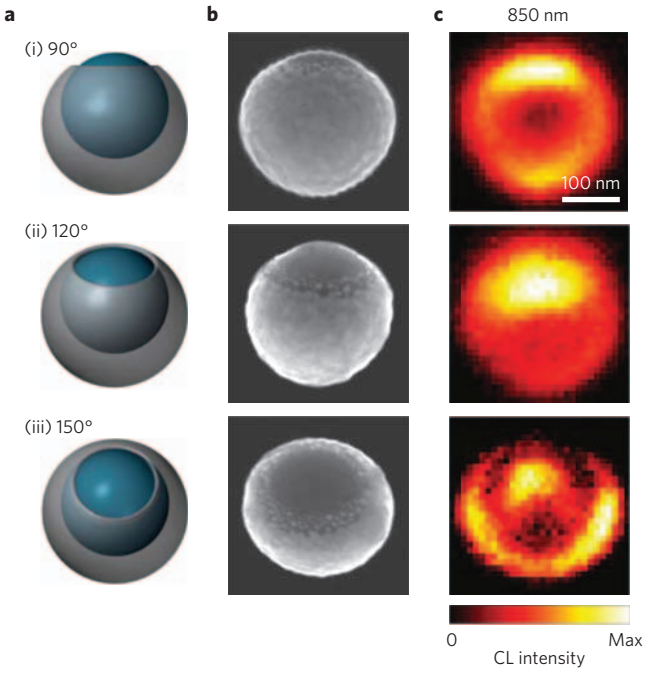

Figure 3 | Two-dimensional cathodoluminescence maps. a, Schematics of crescents with orientations of (i) 90°, (ii) 120° and (iii) 150°. **b**, SEM images of crescents. **c**, Two-dimensional maps of the normalized cathodoluminescence (CL) intensity of crescents at a wavelength of 850 nm. Scale bar: 100 nm (all images).

Fig. 1). The spatial and spectral characteristics of this tip mode are also well reproduced by numerical simulations of cathodoluminescence using the boundary element method (BEM)[44–46] (Supplementary Fig. 6). A discussion of the factors that influence the resolution of the cathodoluminescence technique, including determination of electron–sample interactions via Monte Carlo simulations, is provided in Supplementary Fig. 7.

As the electron beam passes through the base of the crescent (lighter lines in Fig. 2b), the cathodoluminescence signal exhibits a broad peak between ~550 nm and 700 nm. This broad feature is understood by considering three contributions: the high-energy plasmonic resonance supported by the crescent, the contribution of radiation from electron–hole pair recombination in the Au shell, and luminescence from the polystyrene core of the crescent. The higher-energy plasmonic modes exhibit significant field intensity near and inside the base of the crescent, as detailed in Supplementary Fig. 4. However, BEM cathodoluminescence simulations reveal that radiative decay of the high-energy modes alone cannot account for the strong signal at short wavelengths observed in the experiments (Supplementary Fig. 6). By comparing cathodoluminescence spectra to photoluminescence spectra of both crescents and polystyrene cores, we determine that a significant portion of the cathodoluminescence signal at short wavelengths is due to Au[47–49] and polystyrene luminescence[50] (Supplementary Figs 2 and 3).

Before tomographic reconstruction, we probed the effect of crescent angle on cathodoluminescence excitation efficiency. Cathodoluminescence line scans of various crescents at angles between 0° and 165°, in 15° increments, were collected. The normalized cathodoluminescence intensities at 850 nm were used to form the sinogram shown in Fig. 2d. From this sinogram, it was determined that the tip mode at a wavelength of 850 nm is excited for nearly all crescent angles, except for the few angles near 0° and 180°. At these angles, the orientation of the electron beam is perpendicular to the tip gap, which results in inefficient excitation of this mode, as the electron beam preferentially couples to out-of-plane electric-field components, while the tip mode has a strong field oriented across the tips. A sinogram at 550 nm illustrates that cathodoluminescence is excited efficiently near and in the base of the crescent over a broad range of angles, as expected (Supplementary Fig. 4).

By scanning the beam in the SEM and collecting a spectrum at each position, two-dimensional cathodoluminescence maps were generated at all wavelengths concurrently. Figure 3 presents two-dimensional cathodoluminescence maps at a wavelength of 850 nm for crescents at different orientations with respect to the electron beam, as well as schematic representations and SEM images of the crescents. Note that this series of cathodoluminescence maps is the two-dimensional extension of the one-dimensional line scans compiled in the sinogram of Fig. 2d. They confirm that the various modes can be excited for a wide range of crescent angles and allow two-dimensional tracking of radiative optical properties for wavelengths spanning the visible and near-infrared spectrum (Supplementary Fig. 5).

Three-dimensional reconstruction of monochromatic cathodoluminescence

Tomography was then used to map the cathodoluminescence signal from the crescent in three dimensions. The cathodoluminescence maps just discussed, as well as the TEM images, represent two-dimensional projections of a three-dimensional function and, as such, tomography can be used to reconstruct the three-dimensional functions. In the case of the bright-field TEM image, the intensity of the signal is related to the integrated thickness and atomic number of the constituent materials. In cathodoluminescence, the intensity of a given pixel in a two-dimensional map (as in Fig. 3) is proportional to an integral of the cathodoluminescence along the path of the electron. In both cases, for accurate reconstruction, the generated images should satisfy the projection requirement for conventional tomography, which assumes that the signal must be linear and monotonic with the property of interest.

We first reconstructed the three-dimensional structure of the crescent from a transmission electron micrograph to assist in interpretation of the cathodoluminescence tomograms. The intensity of the TEM image is related to the integrated thickness and atomic number of the constituent materials, and rigorously satisfies the projection requirement for our non-crystalline samples. We carried out the reconstruction using a crescent oriented at 90°, as in the TEM image of Fig. 1b. Note that, with this orientation, the axis of rotational symmetry (z) of the crescent is perpendicular to the incident electron beam. As the crescent is assumed to be rotationally symmetric, the single TEM projection of Fig. 1b can be used as a virtual tilt series spanning the full 360° of rotation[51]. To reconstruct the crescent's structure we used the tomographic method of filtered back-projection, which forms a reconstructed image by summing partial reconstructions at various angles[52–54] (Supplementary Section E).

Figure 4a presents the resulting TEM tomographic reconstruction. The black portions of the reconstruction correspond to regions of high atomic number (that is, gold), whereas the dielectric core appears white, similar to the vacuum background (see also Supplementary Fig. 9). In comparing this three-dimensional tomogram with the original TEM image in Fig. 1b, it is clear that reconstruction has resulted in a significantly improved spatial representation of the structure. A very similar tomogram is obtained when two orthogonal tilt series of TEM images are used to reconstruct the crescent structure (Supplementary Fig. 8).

To reconstruct the cathodoluminescence signal, we considered two different tilt series: (1) a virtual tilt series constructed from a single experimental projection utilizing the rotational symmetry of

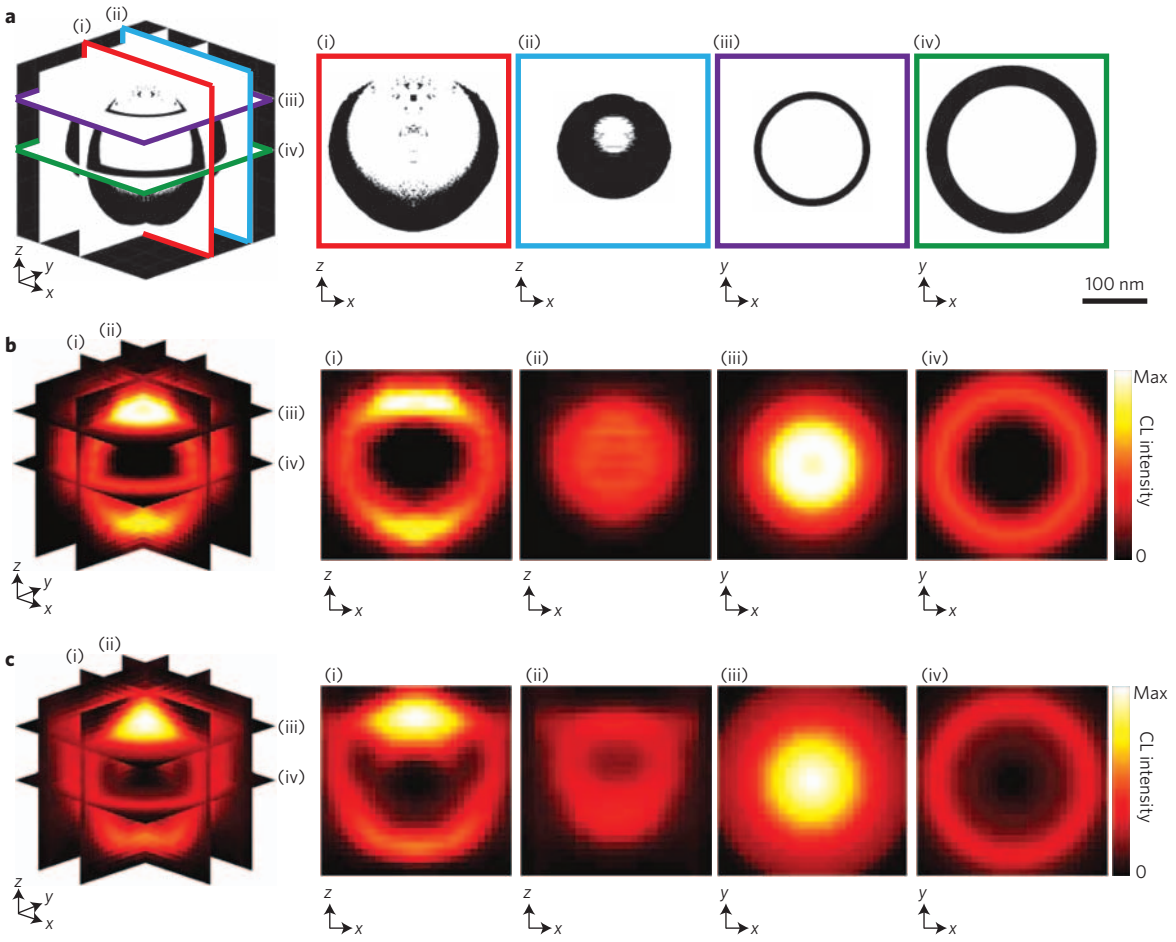

Figure 4 | Three-dimensional TEM and cathodoluminescence reconstructions. a, TEM tomogram based on a single projection. Panels (i) to (iv) correspond to different cross-sections through the reconstruction, as indicated by the coloured outlines. Panel (i) shows an *x*–*z* cross-section of the reconstruction at the midpoint of the crescent, where the metal shell and the crescent geometry can be distinctly resolved. Panel (ii) shows an off-centre *x*–*z* cross-section of the reconstruction for comparison. Panel (iii) is a horizontal *x*–*y* cross-section of the reconstruction at the *z* position where the crescent tips come to a point, and panel (iv) is a *x*–*y* cross-section of the reconstruction at the midpoint of the crescent, clearly showing the metal shell surrounding the inner core. **b**, Cathodoluminescence (CL) tomogram at 850 nm based on a single cathodoluminescence map (reconstruction in *x*–*y* planes). **c**, Cathodoluminescence tomogram at 850 nm based on an experimental tilt series consisting of seven crescents (reconstruction in *x*–*z* planes).

a single crescent and (2) the experimental tilt series of crescents described in Figs 2 and 3. We first used the two-dimensional cathodoluminescence map of Fig. 3c(i) as a virtual tilt series spanning the full 360° of rotation. For this crescent, oriented at 90° with respect to the electron beam (*z*-axis parallel to the substrate), the excited modes are identical for any angle of rotation of the crescent about the *z* axis. While modes that require a *z*-oriented electron beam are not excited in this configuration, the trajectory dependency of the excitation of all other modes is eliminated, as they will contribute uniformly to the cathodoluminescence signal across all tilt angles, allowing for a scalar reconstruction. Note that this use of symmetry to simplify an otherwise complex vector tomography problem is very similar to what was done in previous EELS tomography work[32]. Furthermore, note that material luminescence is a scalar quantity and thus independent of trajectory (within the small particle assumption), and therefore strictly satisfies the projection requirement. In summary, we can use the individual crescent oriented at 90° for a virtual tilt series to directly reconstruct all but the *z* component of the cathodoluminescence signal using conventional scalar tomographic methods. Note that this method assumes negligible particle–substrate interactions, a reasonable assumption for a crescent at $\theta = 90°$, as shown by the simulations provided in Supplementary Figs 10 and 11.

Figure 4b shows the result of a three-dimensional tomographic reconstruction of the cathodoluminescence signal at a wavelength of 850 nm based on reconstructing individual *x*–*y* planes for each value of *z* (for a step-by-step illustration of this technique, see Supplementary Fig. 12). As shown in these figures, the highest cathodoluminescence signal is localized within the gap region between the tips of the crescent. Panels (i) and (iii) in particular illustrate the strong field enhancements that are spatially localized in *z* near the tips, as expected for this mode based on the FDTD simulations shown in Fig. 2c, as well as the BEM simulations provided in Supplementary Fig. 6. Significant cathodoluminescence intensities can also be observed near and around the metallic shell, stemming mostly from the luminescence of the Au itself. A similarly detailed view of the cathodoluminescence reconstruction at a wavelength of 550 nm is provided in Supplementary Fig. 13 for comparison.

To rigorously reconstruct the complete cathodoluminescence signal, including modes excited in all three orthogonal directions, a fully vectorial reconstruction is needed. As no such technique exists at this time, we can approximately reconstruct the full cathodoluminescence signal by carefully considering a tilt series in which the angle between the electron beam and the *z* axis of the crescent is varied. The angular dependence of the excitation of the various modes strictly breaks the projection requirement, but by restricting

the range of angles considered we can minimize this effect. Furthermore, we normalize the tilt series before reconstruction at each wavelength in order to minimize the effect of the variation in excitation efficiency on the reconstruction. Therefore, although the resulting tomogram is not exact, it still provides useful information about the existence and qualitative three-dimensional distribution of all excitable modes in our structure.

We consider cathodoluminescence maps of crescents at different orientations, some of which are shown in Fig. 3. Note that this tilt series is composed of individual crescents at different orientations with respect to the fixed substrate, similar to single-particle analysis in TEM tomography[55], and thus gives information about a mean object. For this tilt series, we obtained two-dimensional cathodoluminescence maps for crescents with angles between 75° and 165°, in 15° increments (which, due to the reflection symmetry of the crescent, are equivalent to angles between 195° and 285°). We chose these angles because particle–substrate interactions are negligible for these crescent orientations.

Reconstruction of the cathodoluminescence signal was then performed using the same filtered back-projection method as before, except that the reconstruction was carried out by two-dimensional reconstruction in the x–z plane for each value of y. Following the example set by previous work[32], we imposed the symmetry of the particle during reconstruction to enhance the quality of the tomogram. Figure 4c shows the result of the three-dimensional reconstruction of the cathodoluminescence signal at a wavelength of 850 nm based on reconstructing individual x–z planes. This experimental multi-crescent reconstruction compares well with the reconstruction from the single projection in Fig. 4b, with all of the main features reproduced: the strong field enhancement near the tips in both (i) and (iii), the reduced areal cross-section in (ii), and the intensity in and around the Au shell in (iv). The remarkable agreement between the two reconstruction schemes, based on two very different sets of initial data, indicates both the validity of the assumption of negligible particle–substrate interactions for the angles considered here, as well as the merits of the qualitative reconstruction scheme. The quality of the multi-crescent reconstruction was also confirmed by comparing the original cathodoluminescence maps to re-projections of the tomograms at the same angles as obtained in the experiment (Supplementary Fig. 15).

Spectroscopic cathodoluminescence tomography

Because cathodoluminescence is a spectroscopic technique, we can reconstruct the cathodoluminescence signal in three dimensions at all wavelengths in the measured 475–950 nm range. Figure 5 plots the reconstructed cathodoluminescence spectra at volumetric pixels, or voxels, along the central axis of the crescent, as indicated in Fig. 5a. Figure 5c,d show the associated spectra for the single- and multi-crescent reconstructions, respectively. By comparing these spectra with the coloured voxels in the schematic, it is clear that the cathodoluminescence spectra vary significantly with position. In the metallic base of the crescent (light pink curves), the cathodoluminescence is strong and peaks broadly between 550 nm and 700 nm. In the dielectric between the tips of the crescent (dark curves), the cathodoluminescence signal peaks again, at ~800 nm to 850 nm. Aside from the discrepancy between the spectra in the dielectric core of the crescent (red curves), which will be discussed in the following, the main spectral trends are visible in both the single- and multi-crescent reconstructions.

The spatially dependent cathodoluminescence can be understood by considering two factors contributing to the intensity of the cathodoluminescence signal in this system: the radiative LDOS within the crescent structure and luminescence from the Au and polystyrene. To investigate the radiative LDOS, which is a measure of the number of radiative decay pathways available to an emitter, we used a FDTD method to calculate the radiative rate

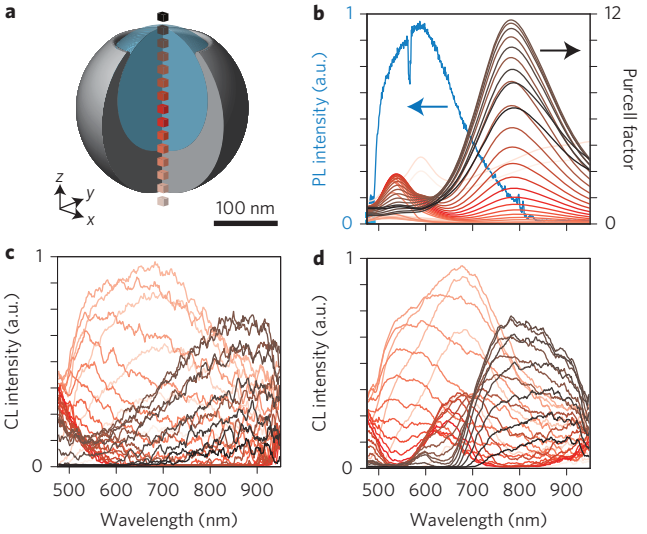

Figure 5 | Axial voxel cathodoluminescence spectra. a, Schematic of voxel positions within the crescent along its central axis. Darker colours correspond to higher z positions. **b**, Total Purcell factor (average of x, y and z components) calculated with FDTD (right axis), and average photoluminescence (PL) spectra of six individual crescents excited at 488 nm (blue curve, left axis). **c**, Voxel spectra from cathodoluminescence (CL) reconstruction based on a single cathodoluminescence map (reconstruction in x–y planes). **d**, Voxel spectra from cathodoluminescence reconstruction based on an experimental tilt series consisting of seven crescents (reconstruction in x–z planes).

enhancement, or Purcell factor (PF), at each position along the crescent axis, as shown in Fig. 5b. These spectra indicate that the radiative LDOS peaks in the gap region between the tips of the crescent at a wavelength of 782 nm. This calculated result is in very good agreement with the peak seen in this spatial region in the reconstructed cathodoluminescence spectra of Fig. 5c,d. Notably, the rapid fall in signal intensity for voxels farther away from the tips is remarkably similar in the calculated PF spectra and the experimental cathodoluminescence spectra. An alternative visualization of these data, together with individual components of the PF, are provided in Supplementary Fig. 16.

Near the metallic base of the crescent, the reconstructed cathodoluminescence signal exhibits a significant and broad peak between 500 nm and 700 nm, which is not fully reproduced in the calculated PF spectra. This feature is also absent from the BEM cathodoluminescence calculations shown in Supplementary Fig. 6. Like the BEM calculations, the PF calculations do not account for material luminescence and, indeed, photoluminescence measurements of individual nanocrescents reveal significant electron–hole pair recombination in the Au shell, as shown in Fig. 5b. The photoluminescence from the Au shell peaks at a wavelength of 593 nm, with a spectral shape that closely resembles the reconstructed cathodoluminescence. The narrower width of the photoluminescence spectrum may be due to the narrowband characteristic of the laser used for photoluminescence experiments (compared to the broadband nature of the electron beam as an excitation source in cathodoluminescence) or to the different temporal characteristics of the excitation. Also, note that the sharp feature at 568 nm is related to the dominant Raman line (-CH_3 symmetric stretch, 2,886 cm^{-1}) of the polydimethylsiloxane (PDMS) substrate used in this photoluminescence experiment[56].

In the dielectric core of the crescent, the multi-crescent reconstruction reveals a peak at ~650 nm not present in the single-crescent reconstruction (compare with Fig. 5c,d). This peak is due to a mode that is not efficiently excited at 90° and therefore does not

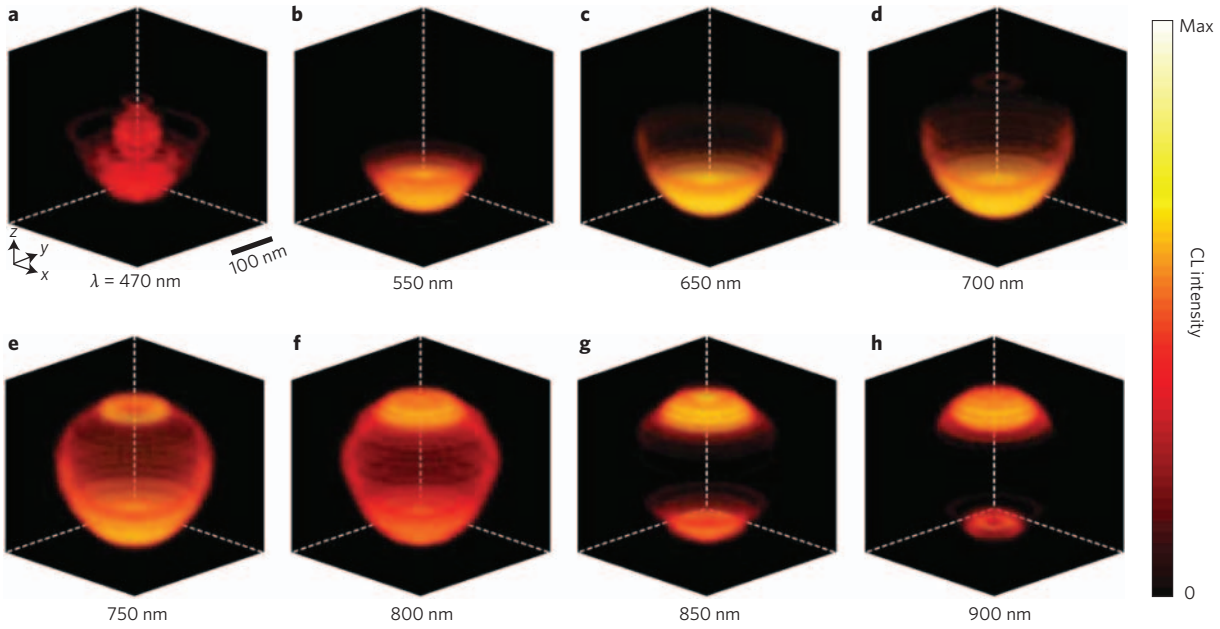

Figure 6 | Cathodoluminescence spectroscopic tomography. a–h, Reconstructed cathodoluminescence (CL) signal based on a single cathodoluminescence map (reconstruction in *x*–*y* planes) at wavelengths of 470 nm (**a**), 550 nm (**b**), 650 nm (**c**), 700 nm (**d**), 750 nm (**e**), 800 nm (**f**), 850 nm (**g**), 900 nm (**h**). The reconstructed intensity corresponds to both the colour scale and the transparency of the figure. Scale bar: 100 nm (all images).

show up in the single-crescent reconstruction, which ignores modes that require a *z*-oriented electron beam for efficient excitation. This mode is identified through plane-wave extinction calculations, BEM cathodoluminescence simulations, as well as PF calculations, which confirm the existence of a mode at ~600 nm excited in the centre of the crescent for a *z*-oriented dipole, but not for *x*- or *y*-oriented dipoles (Supplementary Figs 1 and 17). The existence of this peak in the cathodoluminescence tomogram demonstrates the ability of the multi-crescent reconstruction to probe all modes of the system. Finally, it is interesting to note that the spectra of both reconstruction methods show significant cathodoluminescence signal in the dielectric core of the crescent below 500 nm, rising up to the edge of the spectral window studied here. This signal stems from the luminescence of the polystyrene bead itself[50], which peaks at ~450 nm (see polystyrene photoluminescence spectrum in Supplementary Fig. 3). Taken together, these results demonstrate the high spatial and spectral resolution of the experimental cathodoluminescence reconstructions.

To achieve a complete sense of the spectral and spatial dependence of the cathodoluminescence signal, three-dimensional reconstructions at wavelengths between 470 nm and 900 nm are shown in Fig. 6. In these images, the crescent is oriented with its tips at the tops of the images. This figure contains tomograms generated from the single crescent at 90° (method i); tomograms generated from the experimental multi-crescent tilt series show excellent agreement and are provided in Supplementary Fig. 14. These spectroscopic cathodoluminescence tomograms clearly demonstrate how different spectral features contributing to the cathodoluminescence spectrum of a three-dimensional nanostructure can be resolved at a spatial resolution well below the diffraction limit. Movies illustrating these reconstructions are provided in the Supplementary Information.

Conclusions

In summary, we have developed cathodoluminescence spectroscopic tomography as a novel technique to probe deeply subwavelength radiative optical properties in three dimensions. The technique allows spectral reconstruction of individual nanoscale volumetric pixels, spanning visible and near-infrared frequencies. The resultant tomograms reveal regions of efficient cathodoluminescence, with contributions from both material luminescence and radiative decay of resonant electromagnetic modes. Looking forward, we envision cathodoluminescence tomographic reconstructions that include momentum- and polarization-resolved information with nanometre-scale voxel resolution. Additionally, the application of cathodoluminescence tomography to systems beyond simple inorganic specimens should be straightforward. For example, this tomographic technique could be used to precisely locate radiative recombination centres in light-emitting diodes, probe the nanoscale distribution of defect states in organic photovoltaics, and potentially provide new label-free avenues for biological imaging.

Methods

Crescent fabrication. Nanocrescents were fabricated by metal evaporation onto dielectric beads. An aqueous solution of 200-nm-diameter polystyrene beads (Polysciences, coefficient of variance = 8%) was deposited onto a glass coverslip coated with polydiallydimethylammonium chloride, a charged polymer used to improve areal coverage. The coverslip was then mounted on a rotation stage tilted at an angle of ~45° and rotated at 45 r.p.m. during electron-beam evaporation. Gold was evaporated at a rate of ~1 Å s^{-1} until the thickness of the metal at the base of the dielectric beads reached ~70 nm. For TEM, the crescents were removed from the substrate with a carbon grid coated with an ultra-thin layer of PDMS. For cathodoluminescence experiments, the crescents were removed from the original substrate with a PDMS stamp and then transferred onto a clean Si wafer via a transfer printing procedure that, importantly, did not preserve their orientation. The orientation of each crescent was determined by taking SEM images at a stage tilt of 0° and 40°, and the images were compared to a computer-generated tilt series.

TEM imaging. TEM images were obtained using an FEI Tecnai G2 F20 X-TWIN transmission electron microscope at 200keV in bright-field imaging mode.

Cathodoluminescence spectroscopy. Cathodoluminescence measurements were performed in an FEI XL-30 SFEG SEM with an aluminium paraboloid mirror attached to a piezoelectric positioning system. The 30 keV electron beam passed through a 600 μm hole in the mirror, directly above its focal point. The beam spot diameter was ~10 nm and the typical beam current used was ~1 nA. Emitted radiation was collected by the mirror and passed outside the microscope into a spectrometer fitted with a liquid-nitrogen-cooled Si charge-coupled device detector.

To generate one-dimensional and two-dimensional cathodoluminescence maps, the beam was incrementally scanned and a spectrum was collected at each position. For all cathodoluminescence experiments, the electron beam step size, and therefore the pixel size, was 10 nm. The cathodoluminescence spectra and sinogram in Fig. 2,

which represent line scans through crescents, were smoothed by averaging the central three pixel lines (30 nm) of the two-dimensional map, as well as by averaging over wavelengths in a ±5 nm range. Spectral noise in the cathodoluminescence maps and tomograms was reduced by averaging over wavelengths in a ±5 nm range.

Numerical simulations. Plane-wave and dipole excitation of the crescent were modelled using three-dimensional FDTD methods, with the software 'FDTD Solutions' by Lumerical Solutions. Electron-beam excitation was modelled using the BEM[44–46]. In all cases, the simulated crescent had the following geometrical parameters: 270-nm-diameter Au shell (permittivity from the *CRC Handbook of Chemistry and Physics*); 200-nm-diameter dielectric core (index = 1.47), offset in the $+z$ direction by 32.5 nm; 145-nm-diameter tip gap; 5.5 nm radius of curvature of the tips; 1 nm mesh size. The extinction cross-section under plane-wave excitation was calculated as the sum of the scattering and absorption cross-sections using a total-field–scattered-field source approach. The PF for a given position and orientation was calculated as the ratio of the power emitted to the far field by a dipole to the power emitted by a dipole in free space. The total PF at a given position was calculated by averaging the contributions from the three orthogonal orientations.

Tomographic reconstruction. The method of filtered back-projection was used to reconstruct three-dimensional functions from two-dimensional projections. A ramp filter multiplied by a Hann window was used both to increase the contrast and to decrease the noise in the reconstructions. Complete details are provided in the Supplementary Information.

Photoluminescence. Photoluminescence spectra were collected from individual crescents on a PDMS substrate, using a focused continuous-wave Ar-ion laser operated at 488 nm. The photoluminescence spectrum shown in Fig. 5b represents the average of six normalized single-particle spectra. Dark-field scattering spectra were collected before and after laser illumination to guarantee that the crescents had not been damaged during the experiment.

Received 14 August 2014; accepted 9 February 2015;
published online XX XX 2015

References

1. Arridge, S. R. Optical tomography in medical imaging. *Inverse Problems* **15,** R41 (1999).
2. Munk, W., Worcester, P. & Wunsch, C. *Ocean Acoustic Tomography* (Cambridge Univ. Press, 2009).
3. Nolet, G. (ed.) *Seismic Tomography* (Springer Netherlands, 1987).
4. Crowther, R. A., DeRosier, D. J. & Klug, A. The reconstruction of a three-dimensional structure from projections and its application to electron microscopy. *Proc. R. Soc. Lond. A* **317,** 319 (1970).
5. Yao, N. & Wang, Z. L. *Handbook of Microscopy for Nanotechnology* (Springer, 2006).
6. Midgley, P. A. & Dunin-Borkowski, R. E. Electron tomography and holography in materials science. *Nature Mater.* **8,** 271 (2009).
7. De Winter, D., Lebbink, M. N., Wiggers De Vries, D. F., Post, J. A. & Drury, M. R. FIB–SEM cathodoluminescence tomography: practical and theoretical considerations. *J. Microsc.* **243,** 315 (2011).
8. Van Aert, S., Batenburg, K. J., Rossell, M. D., Erni, R. & Van Tendeloo, G. Three-dimensional atomic imaging of crystalline nanoparticles. *Nature* **470,** 374 (2011).
9. Scott, M. C. *et al.* Electron tomography at 2.4-ångström resolution. *Nature* **483,** 444 (2012).
10. Möbus, G., Doole, R. C. & Inkson, B. J. Spectroscopic electron tomography. *Ultramicroscopy* **96,** 433 (2003).
11. Gass, M. H., Koziol, K. K. K., Windle, A. H. & Midgley, P. A. Four-dimensional spectral tomography of carbonaceous nanocomposites. *Nano Lett.* **6,** 376 (2006).
12. Jarausch, K., Thomas, P., Leonard, D. N., Twesten, R. & Booth, C. R. Four-dimensional STEM-EELS: enabling nano-scale chemical tomography. *Ultramicroscopy* **109,** 326 (2009).
13. Haberfehlner, G. *et al.* Four-dimensional spectral low-loss energy-filtered transmission electron tomography of silicon nanowire-based capacitors. *Appl. Phys. Lett.* **101,** 063108 (2012).
14. Huang, B., Wang, W., Bates, M. & Zhuang, X. Three-dimensional super-resolution imaging by stochastic optical reconstruction microscopy. *Science* **319,** 810 (2008).
15. Pavani, S. R. P. *et al.* Three-dimensional, single-molecule fluorescence imaging beyond the diffraction limit by using a double-helix point spread function. *Proc. Natl. Acad. Sci. USA* **106,** 2995 (2009).
16. Klar, T. *et al.* Surface-plasmon resonances in single metallic nanoparticles. *Phys. Rev. Lett.* **80,** 4249 (1998).
17. Schnell, M. *et al.* Controlling the near-field oscillations of loaded plasmonic nanoantennas. *Nature Photon.* **3,** 287 (2009).
18. Fei, Z. *et al.* Gate-tuning of graphene plasmons revealed by infrared nano-imaging. *Nature* **487,** 82 (2012).
19. Chen, J. *et al.* Optical nano-imaging of gate-tunable graphene plasmons. *Nature* **487,** 77 (2012).
20. Michaelis, J., Hettich, C., Mlynek, J. & Sandoghdar, V. Optical microscopy using a single-molecule light source. *Nature* **405,** 325 (2000).
21. Farahani, J. N., Pohl, D. W., Eisler, H. J. & Hecht, B. Single quantum dot coupled to a scanning optical antenna: a tunable superemitter. *Phys. Rev. Lett.* **95,** 017402 (2005).
22. Frimmer, M., Chen, Y. & Koenderink, A. F. Scanning emitter lifetime imaging microscopy for spontaneous emission control. *Phys. Rev. Lett.* **107,** 123602 (2011).
23. Dolde, F. *et al.* Electric-field sensing using single diamond spins. *Nature Phys.* **7,** 459 (2011).
24. Geiselmann, M. *et al.* Three-dimensional optical manipulation of a single electron spin. *Nature Nanotech.* **8,** 175 (2013).
25. García de Abajo, F. J. Optical excitations in electron microscopy. *Rev. Mod. Phys.* **82,** 209 (2010).
26. García de Abajo, F. & Kociak, M. Probing the photonic local density of states with electron energy loss spectroscopy. *Phys. Rev. Lett.* **100,** 106804 (2008).
27. Hohenester, U., Ditlbacher, H. & Krenn, J. R. Electron-energy-loss spectra of plasmonic nanoparticles. *Phys. Rev. Lett.* **103,** 106801 (2009).
28. Yamamoto, N., Araya, K. & García de Abajo, F. Photon emission from silver particles induced by a high-energy electron beam. *Phys. Rev. B* **64,** 205419 (2001).
29. Coenen, T., Vesseur, E., Polman, A. & Koenderink, A. Directional emission from plasmonic Yagi-uda antennas probed by angle-resolved cathodoluminescence spectroscopy. *Nano Lett.* **11,** 3779 (2011).
30. Sapienza, R. *et al.* Deep-subwavelength imaging of the modal dispersion of light. *Nature Mater.* **11,** 781 (2012).
31. Hörl, A., Trügler, A. & Hohenester, U. Tomography of particle plasmon fields from electron energy loss spectroscopy. *Phys. Rev. Lett.* **111,** 076801 (2013).
32. Nicoletti, O. *et al.* Three-dimensional imaging of localized surface plasmon resonances of metal nanoparticles. *Nature* **502,** 80 (2013).
33. Aubry, A. *et al.* Plasmonic light-harvesting devices over the whole visible spectrum. *Nano Lett.* **10,** 2574 (2010).
34. Fernandez-Dominguez, A. I., Luo, Y., Wiener, A., Pendry, J. & Maier, S. A. Theory of three-dimensional nanocrescent light harvesters. *Nano Lett.* **12,** 5946 (2012).
35. Luo, Y., Lei, D. Y., Maier, S. A. & Pendry, J. Broadband light harvesting nanostructures robust to edge bluntness. *Phys. Rev. Lett.* **108,** (2012).
36. Lu, Y., Liu, G., Kim, J., Mejia, Y. & Lee, L. Nanophotonic crescent moon structures with sharp edge for ultrasensitive biomolecular detection by local electromagnetic field enhancement effect. *Nano Lett.* **5,** 119 (2005).
37. Liu, G. L., Lu, Y., Kim, J., Doll, J. C. & Lee, L. P. Magnetic nanocrescents as controllable surface-enhanced Raman scattering nanoprobes for biomolecular imaging. *Adv. Mater.* **17,** 2683 (2005).
38. Ross, B. & Lee, L. Plasmon tuning and local field enhancement maximization of the nanocrescent. *Nanotechnology* **19,** 275201 (2008).
39. Knight, M. W. & Halas, N. J. Nanoshells to nanoeggs to nanocups: optical properties of reduced symmetry core–shell nanoparticles beyond the quasistatic limit. *New J. Phys.* **10,** 105006 (2008).
40. Atre, A. C., García-Etxarri, A., Alaeian, H. & Dionne, J. A. Toward high-efficiency solar upconversion with plasmonic nanostructures. *J. Opt.* **14,** 024008 (2012).
41. Cortie, M. & Ford, M. A plasmon-induced current loop in gold semi-shells. *Nanotechnology* **18,** 235704 (2007).
42. Mirin, N. A. & Halas, N. J. Light-bending nanoparticles. *Nano Lett.* **9,** 1255 (2009).
43. Atre, A. C., García-Etxarri, A., Alaeian, H. & Dionne, J. A. A broadband negative index metamaterial at optical frequencies. *Adv. Opt. Mater.* **1,** 327 (2013).
44. García de Abajo, F. & Howie, A. Relativistic electron energy loss and electron-induced photon emission in inhomogeneous dielectrics. *Phys. Rev. Lett.* **80,** 5180 (1998).
45. García de Abajo, F. & Howie, A. Retarded field calculation of electron energy loss in inhomogeneous dielectrics. *Phys. Rev. B* **65,** 115418 (2002).
46. Gómez-Medina, R., Yamamoto, N., Nakano, M. & García de Abajo, F. J. Mapping plasmons in nanoantennas via cathodoluminescence. *New J. Phys.* **10,** 105009 (2008).
47. Mooradian, A. Photoluminescence of metals. *Phys. Rev. Lett.* **22,** 185 (1969).
48. Wu, X. *et al.* High-photoluminescence-yield gold nanocubes: for cell imaging and photothermal therapy. *ACS Nano* **4,** 113 (2009).
49. Yorulmaz, M., Khatua, S., Zijlstra, P., Gaiduk, A. & Orrit, M. Luminescence quantum yield of single gold nanorods. *Nano Lett.* **12,** 4385 (2012).
50. George, G. A. The phosphorescence spectrum and photodegradation of polystyrene films. *J. Appl. Polym. Sci.* **18,** 419 (1974).
51. Hanson, K. M. Special topics in test methodology: tomographic reconstruction of axially symmetric objects from a single radiograph. *Progr. Astronaut. Aeronaut.* **155,** 1 (1993).
52. Wang, X. Y. *et al.* Reconstruction and visualization of nanoparticle composites by transmission electron tomography. *Ultramicroscopy* **113,** 96 (2012).
53. Lyra, M. & Ploussi, A. Filtering in SPECT image reconstruction. *Int. J. Biomed. Imag.* **2011,** 1 (2011).

54. Arslan, I., Tong, J. R. & Midgley, P. A. Reducing the missing wedge: high-resolution dual axis tomography of inorganic materials. *Ultramicroscopy* **106,** 994 (2006).
55. Van Heel, M. *et al*. Single-particle electron cryo-microscopy: towards atomic resolution. *Q. Rev. Biophys.* **33,** 307 (2000).
56. Cai, D., Neyer, A., Kuckuk, R. & Heise, H. M. Raman, mid-infrared, near-infrared and ultraviolet–visible spectroscopy of PDMS silicone rubber for characterization of polymer optical waveguide materials. *J. Mol. Struct.* **976,** 274 (2010).

Acknowledgements

The authors thank S. Sheikholeslami and A. Saleh for assistance with photoluminescence measurements, and J. Briggs and T. Narayan for scientific discussions. The authors also thank T. Carver for electron beam evaporation. A.C.A. acknowledges support from the Robert L. and Audrey S. Hancock Stanford Graduate Fellowship. J.A.D. acknowledges support from an Air Force Office of Scientific Research Young Investigator Grant (FA9550-11-1-0024) and a National Science Foundation CAREER Award (DMR-1151231). Funding from a Department of Energy EERE Sunshot grant (no. DE-EE0005331) is also acknowledged. This work is part of the research programme of the Stichting voor Fundamenteel Onderzoek der Materie (FOM), which is supported financially by the Nederlandse Organisatie voor Wetenschappelijk Onderzoek (NWO). This work was funded by the European Research Council and is also part of NanoNextNL, a nanotechnology programme funded by the Dutch Ministry of Economic Affairs.

Author contributions

A.C.A. fabricated samples and performed transmission electron microscopy, photoluminescence spectroscopy, tomographic reconstruction and electromagnetic simulations. A.C.A., B.J.M.B. and T.C. performed the cathodoluminescence microscopy, spectroscopy and scanning electron microscopy. A.G-E. performed boundary element method simulations. J.A.D. and A.P. guided and supervised the experiments and analysis. All authors analysed and interpreted the results and edited the manuscript.

Additional information

Supplementary information is available in the online version of the paper. Reprints and permissions information is available online at www.nature.com/reprints. Correspondence and requests for materials should be addressed to A.C.A.

Competing financial interests

The authors declare no competing financial interests.

SUPPLEMENTARY INFORMATION

Nanoscale optical tomography with cathodoluminescence spectroscopy

Ashwin C. Atre,[1] Benjamin J.M. Brenny,[2] Toon Coenen,[2] Albert Polman,[2] and Jennifer A. Dionne[1]

[1)] *Department of Materials Science and Engineering, Stanford University, Stanford, CA 94305, USA*

[2)] *Center for Nanophotonics, FOM Institute AMOLF, Science Park 104, 1098 XG Amsterdam, The Netherlands*

A. Calculating nanocrescent modes

The plasmonic modes of the crescent are determined by exciting the structure with plane waves in finite difference time domain (FDTD) simulations. The extinction efficiency, the ratio of the extinction cross section to the geometrical cross section, is calculated for various angles of incidence, θ, where θ is the angle between the crescent's axis of symmetry and the polarization of the electric field in the (x, z) plane. The extinction spectra for angles between 0° and 90° in 15° increments are shown in Figure S1(a).

A number of different modes can be identified from the spectra. The lowest energy mode at 874 nm, excited most efficiently at 90°, is characterized by strong electric field enhancement between the sharp tips of the crescent. This mode peaks at approximately 850 nm in the CL experiments, in excellent agreement with the simple model. The nature of this mode is illustrated in Figures S1(b)-(e), which plot the calculated intensity of the scattered electric field at 874 nm for a crescent oriented at 90° at various slices, as indicated in the color-coded schematic in Figure S1(a). Figure S1(b) plots the central cross section in the (x, z) plane, as given in the main text. Figure S1(c) plots the central cross section in the (y, z) plane, orthogonal to the direction of electric field polarization. Figures S1(d) and (e) plot cross sections in the (x, y) plane at the position of the tip gap and at the center of the crescent, respectively. Note that these cross sections correspond to the slices of the reconstruction given in Figures 4 (i), (iii), and (iv) of the main text. From the simulated cross sections shown here, it can be seen that this mode is characterized by strong field enhancement primarily between the tips of the crescent, which agrees well with the experimental CL tomogram.

B. Cathodoluminescence signal at high energies

To understand the peaks in the CL spectra at high energies, we must consider not only the radiative decay of plasmonic modes, but also the luminescence from Au and polystyrene. Radiation in Au occurs when an electron in the d band is excited to an unoccupied state in the sp conduction band. Some fraction of these excited electrons recombine radiatively with the holes in the d band, resulting in emission of a visible photon. This interband transition process is typically studied by exciting the Au with light using photoluminescence (PL)

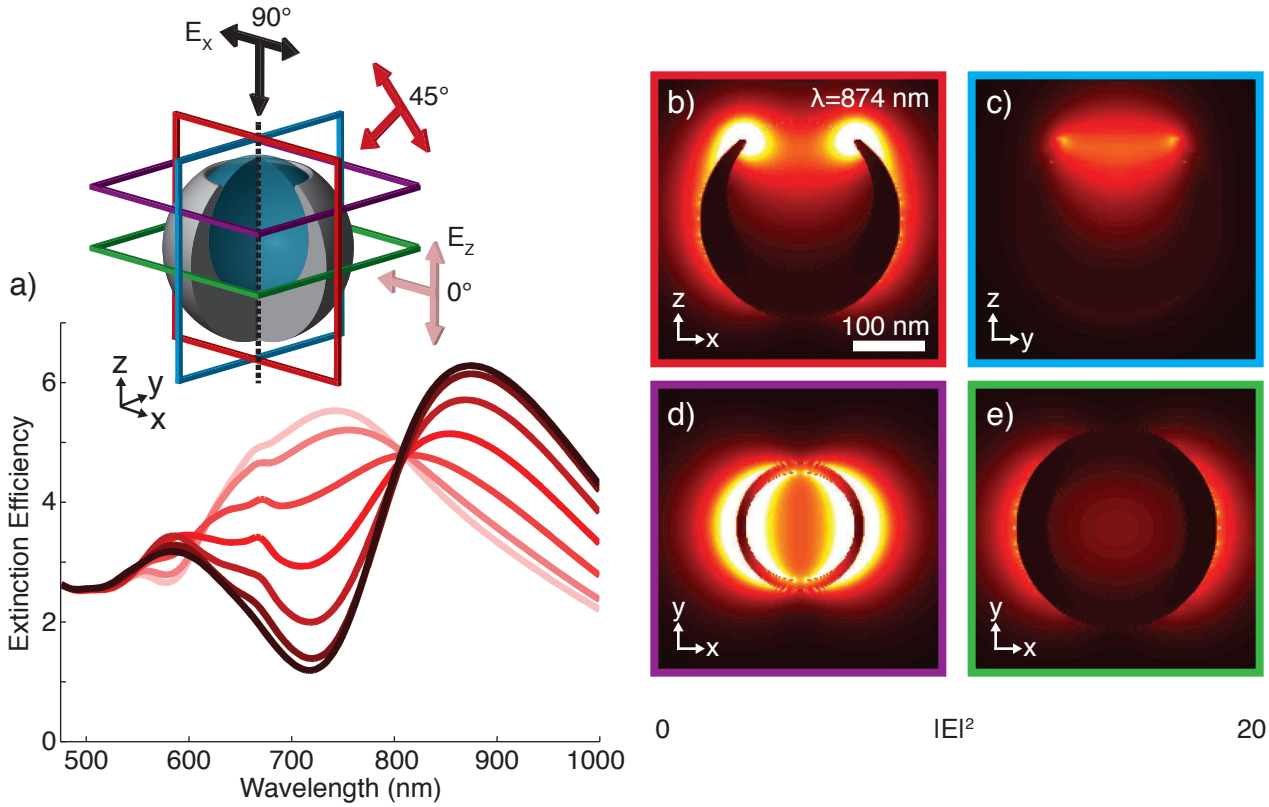

FIG. S1. **Plane wave excitation** a) The extinction efficiency, calculated using FDTD, for plane waves at angles of incidence between 0° (light pink curve) and 90° (black curve), in 15° increments. The scattered electric field intensity at 874 nm of a crescent at 90° for cross sections of: b) the central slice in the (x, z) plane, c) the central slice in the (y, z) plane, d) a slice through the tips in the (x, y) plane, and e) a slice through the center in the (x, y) plane. The slices in (b)-(e) are color-coded according to the schematic in (a). Scale bar of 100 nm applies to all field maps.

spectroscopy. For smooth Au films[1], the PL quantum yield is as low as 10^{-10}, and this source of radiation is therefore often ignored in many CL experiments[2]. However, it has been shown that nanoparticles of Au exhibit PL quantum yields as high as 0.04, more than eight orders of magnitude higher than Au films[3–8].

To demonstrate that radiation from electron-hole pair recombination in Au contributes to the CL signal of crescents, we consider both CL and PL from crescents in Figure S2. Figure S2(a) shows a TEM image of a crescent, where, due to mass-thickness contrast, the intensity corresponds to the amount of Au at each location. We plot a line scan of the TEM intensity along the central axis in Figure S2(b), where it can be seen that the Au

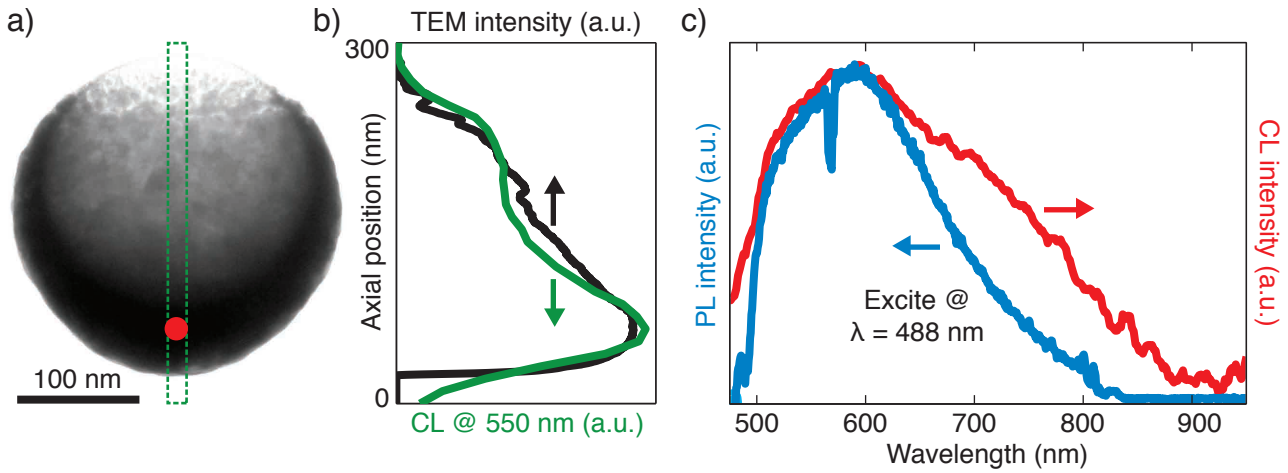

FIG. S2. **Au luminescence.** a) TEM of crescent. b) Axial line scans of both TEM intensity (black curve) and CL intensity at 550 nm (green curve) for the region identified by the green box in (a). c) Average photoluminescence (PL) spectrum of six individual crescents when excited at 488 nm (blue curve), as well as the CL spectrum from inside the base of the crescent at the position identified by the red dot in (a), derived from the CL tomogram.

density peaks in the base of the crescent, as expected for this geometry. Overlaid in the figure is a line scan of the measured CL intensity along the central axis at a wavelength of 550 nm, where Au is known to fluoresce. By comparing these two curves, we see that the CL intensity at 550 nm tracks the Au density quite well. The fact that this CL signal is correlated with the amount of Au the electron interacts with suggests that luminescence from Au contributes significantly to the CL signal at this wavelength.

To confirm this hypothesis, we measure the PL of individual crescents excited at 488 nm with a CW Ar-ion laser. An average of six single crescent PL spectra is shown in Figure S2(c). The sharp feature at 568 nm is due to the dominant Raman line (-CH_3 symmetric stretch, 2886 cm^{-1}) of the polydimethylsiloxane (PDMS) substrate used in this experiment[9], which shows up as a dip in the spectrum due to imperfect background subtraction. On top of this spectrum we plot the CL spectrum at the axial position in the base of the crescent where the peak Au density is found in Figure S2(b), as indicated by the red dot in Figure S2(a). This CL spectrum is from the multi-crescent reconstruction (method (ii)), as explained in the text. Both the PL and the CL spectra peak near 595 nm, and exhibit similar spectral shapes. The increased breadth of the CL spectrum may be due to the broadband nature of the electron

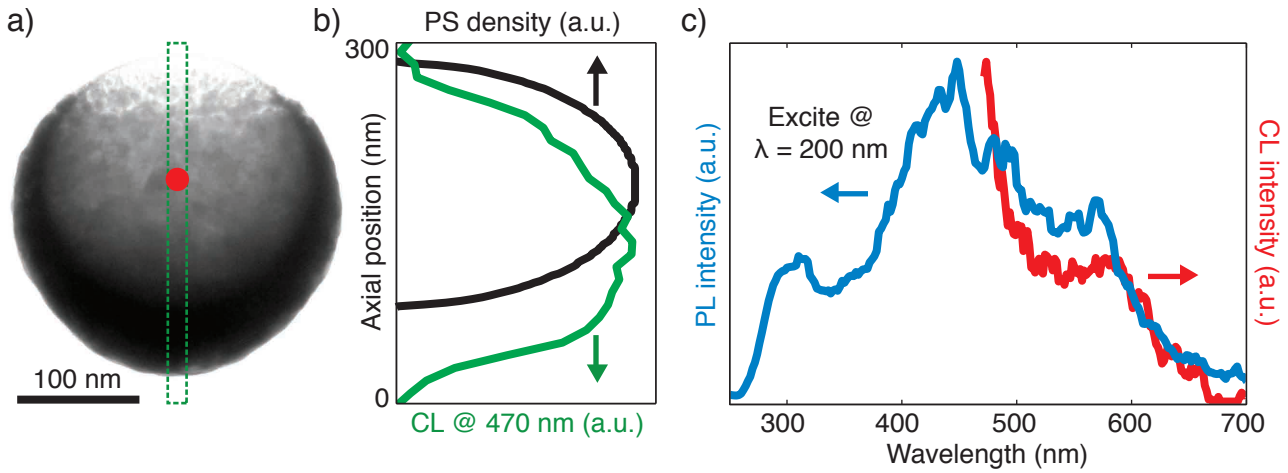

FIG. S3. **Polystyrene luminescence.** a) TEM of crescent. b) Axial line scans of both polystyrene (PS) density (from model, black curve) and CL intensity at 470 nm (green curve) for the region identified by the green box in (a). c) Photoluminescence spectra of 200 nm diameter polystyrene beads (used as the dielectric core of the crescent) when excited at a wavelength of 200 nm (blue curve), as well as the CL spectrum from inside the polystyrene core of the crescent at the position identified by the red dot in (a), derived from the CL tomogram.

beam as an excitation source, as compared to the extremely narrowband characteristic of the laser used for PL experiments, or due to the different temporal characteristics of the excitation.

The strong spatial agreement of Figure S2(b) and spectral agreement of Figure S2(c) suggest that radiation due to electron-hole pair recombination in Au is responsible for a significant portion of the crescent CL signal at short wavelengths.

Another source of CL at the shortest wavelengths probed in this experiment is luminescence from the polystyrene core of the crescent, as shown in Figure S3. A TEM image of a crescent is given in Figure S3(a) for reference. Once again focusing on the central axis of the crescent, we plot a line scan of the density of polystyrene in Figure S3(b), calculated based on the crescent geometry used in FDTD simulations. This is compared to a line scan of the CL intensity along the central axis at a wavelength of 470 nm, at which polystyrene is known to photoluminesce[10]. While some signal at this wavelength is likely due to Au luminescence and radiative decay of the high energy plasmonic modes, the shape of the CL spectrum suggests that a portion of the signal is originating from the dielectric core,

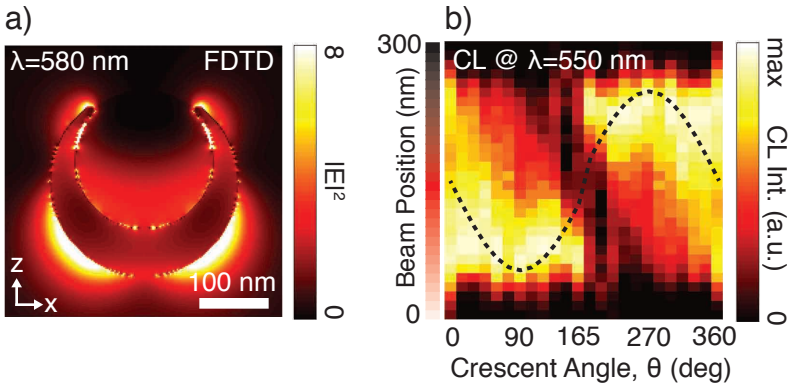

FIG. S4. **High energy crescent mode** a) Central cross-section of the intensity of the scattered electric field for a plane wave incident along $-z$, polarized along x, at a wavelength of 580 nm. The largest enhancement is concentrated near the base of the crescent at this wavelength. b) Experimental sinogram of normalized CL intensity line scans at 550 nm. The dashed line tracks the position of the center of the base of the crescent.

especially in comparing Figure S3(b) with Figure S2(b).

To confirm that the 200 nm diameter polystyrene beads used as the core of the crescents exhibit PL in this spectral regime, we perform PL measurements of polystyrene beads suspended in water using a Cary Eclipse fluorescence spectrophotometer. The excitation is centered at a wavelength of 200 nm and the emission is collected after a delay of one microsecond to avoid Raman scattering. The PL spectrum, smoothed by averaging over neighboring wavelengths in a ±5 nm range, is given in Figure S3(c), and is seen to peak at 450 nm, in good agreement with previous studies. Also plotted in this figure is the CL spectrum from the single-crescent reconstruction, at the axial position at the center of the polystyrene core of the crescent, as indicated by the red dot in Figure S3(a). In comparing these spectra, it is important to keep in mind that the luminescence of polystyrene will be modified by the presence of the Au shell. Although the PL from polystyrene beads is relatively broad, CL signal is only clearly observed within the dielectric bead in the 3D tomograms (Figure 6 of the main text) at the shortest wavelengths because radiation from the Au shell becomes dominant beyond 500 nm.

Of course understanding the plasmonic resonances supported by the crescent at these short wavelengths is also important when interpreting the CL signal, as radiative decay of these modes will contribute to the overall CL signal. The nature of the high energy crescent

mode is elucidated by plotting the intensity of the scattered electric field at 580 nm, the peak in the extinction efficiency at high energies, when illuminated with a field polarized in the x-direction, as shown in Figure S4(a). It can be seen that the field enhancement is localized to the base of the crescent, both inside and outside of the metal shell. This is in contrast to the lowest energy mode at 874 nm, which exhibits the highest field intensity between the tips of the crescent. The high energy mode localized near the metallic base, while also excited directly by the electron beam, most likely enhances the radiation from Au near the base of the crescent.

The physical localization of this high energy CL signal is confirmed by examining the CL tilt series. CL line scans of crescents at angles between 0° and 165°, in 15° increments, are collected, and the normalized intensities at 550 nm are used to form the sinogram shown in Figure S4(b). Here, the dashed sine curve overlay denotes the physical position of the center of the base of the crescent, derived from the crescent model, which roughly tracks the location of the CL signal, as expected for the high energy crescent mode. The downward sloping streak of low CL intensity in the middle of the sinogram corresponds to regions where the electron passes through relatively little Au, and consequently where less Au luminescence is emitted at this wavelength. This sinogram therefore suggests that the high energy CL signal is comprised of both radiative decay of the high energy crescent mode as well as radiation from electron-hole pair recombination in Au.

CL maps of crescents with different orientations help illustrate this point more completely. Figure S5 shows schematics, SEM images, and 2D CL maps at 550 nm for crescents at angles of 90°, 120°, and 150°, respectively. The CL maps allow us to visualize where the most efficient excitation occurs at this short wavelength. As expected, across all crescent angles, the CL signal is highest towards the base of the crescent and where the Au is thickest. Note that these maps are part of a tilt-series of 7 crescents used to reconstruct the CL signal in three dimensions via tomography.

Another way to understand the spatial and spectral dependence of crescent CL is to compare CL line scans of crescents at different angles, as given in Figure S5(d) for angles of 90°, 120°, and 150°. Here, the color of the different spectra correspond to the different excitation positions indicated in Figure S5(a). At short wavelengths, the CL peaks consistently near the base of the crescent (light pink lines) where the high energy modes are excited and where the metal shell is at its thickest. At longer wavelengths, the peak centered in the 800–

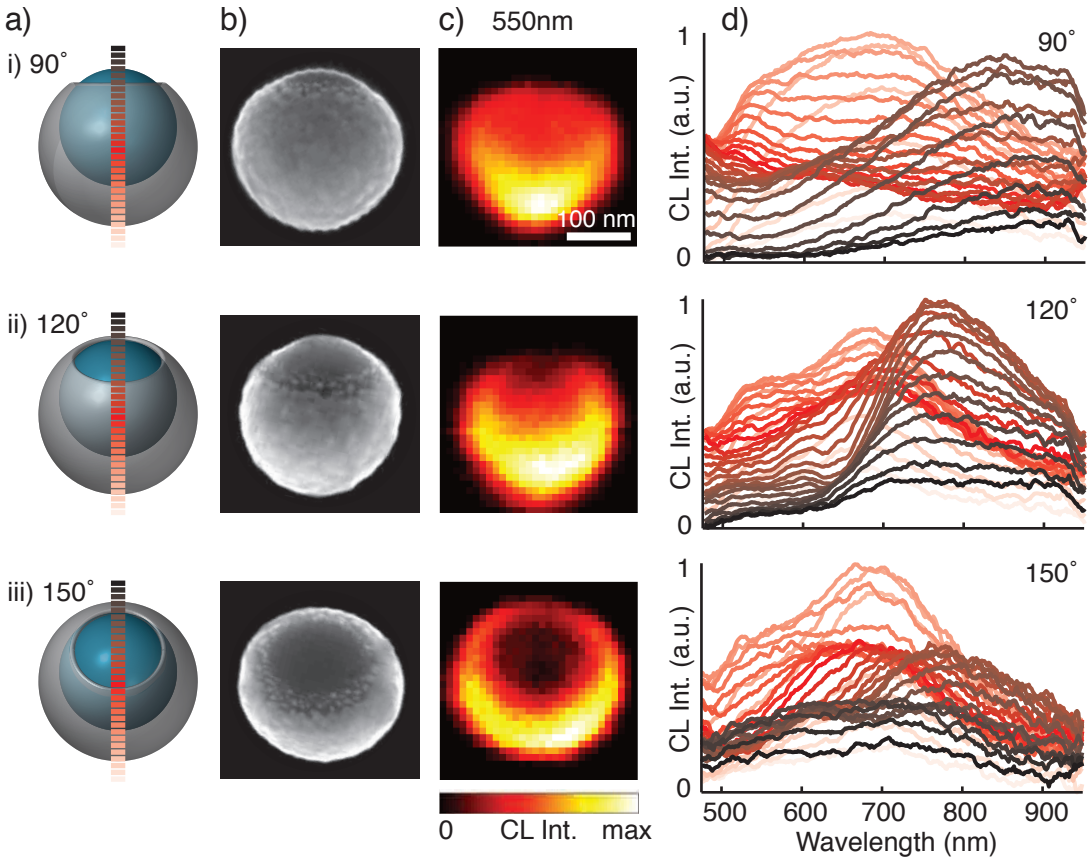

FIG. S5. **Crescent CL tilt series** a) Schematics of crescents at various orientations, where the angle between the crescent's axis of symmetry and the electron beam is i) 90°, ii) 120°, and iii) 150°. b) SEM images of crescents. c) CL maps of crescents at a wavelength of 550 nm. Scale bar of 100 nm applies to all images. d) Experimental CL line scans of crescents where the line colors correspond to the excitation positions indicated in (a).

850 nm spectral range (dark brown curves) decreases in magnitude for increasing crescent angle. This is due to reduced coupling to this mode at 180° (or 0°) when the electron beam is parallel to the crescent's axis of symmetry. However, this mode is excited at most angles, and the slight shift in spectral position is likely due to small differences in the geometry of the sharp tips. The excitation of this mode across nearly all crescent angles is most clearly seen in the CL sinogram at 850 nm given in the main text, which consists of 12 different crescent angles.

C. Tomographic reconstruction by filtered back projection

Tomography has been used for nearly a century as a method for creating a 2D (3D) image of an object based on a series of 1D (2D) projections. A detailed derivation of the method can be found elsewhere[11–13], but a brief summary of tomographic reconstruction in two dimensions based on filtered back projection will be presented here.

Consider a function $f(x, y)$ to be reconstructed. A line L which sits a distance p away from the origin and whose normal forms an angle θ with the x axis can be described by the parametric equation $p = x\cos\theta + y\sin\theta$. The projection of the function f at angle θ is defined as the line integral of f along L, and is known as the Radon transform

$$g_\theta(p) = \int_{y=-\infty}^{\infty} \int_{x=-\infty}^{\infty} f(x, y)\delta(x\cos\theta + y\sin\theta - p)dxdy \tag{1}$$

where the projection vector g_θ is composed of line integrals along lines parallel to L at various values of p.

Next, this projection vector is converted into the frequency domain to allow filtering by multiplication rather than convolution. The projection vector in the discrete Fourier domain is calculated with a Fourier transform, and is given by

$$G_\theta = \sum_{n=0}^{N-1} g_{\theta,n}\exp\left(-\frac{i2\pi kn}{N}\right) \qquad k = 0, 1, ..., N-1 \tag{2}$$

where N is the number of points in the original projection vector.

This function is then multiplied by a frequency filter, H, resulting in a filtered projection in the frequency domain, $\widetilde{G} = GH$, where the tilde indicates a filtered function. The filter is chosen to reduce the contribution of low frequencies while boosting higher frequencies, ultimately yielding a sharper back projection. The simplest version of such a filter is a ramp filter, whose frequency response is given by $|\nu|$. To reduce high frequency noise, however, this ramp filter is multiplied by a low pass filter, a window function that tails off at higher frequencies. Here we use a Hann window, resulting in an overall frequency filter of

$$H = \nu\left(0.5\left(1 - \cos\left(\pi\frac{\nu - \nu_{max}}{\nu_{max}}\right)\right)\right) \qquad 0 \le \nu \le \nu_{max} \tag{3}$$

where ν_{max} is chosen to be the sampling frequency, which is determined by the resolution of the original projections.

The filtered projection is returned back to the spatial domain by taking the real part of the inverse discrete Fourier transform of $\widetilde{G}$

$$\widetilde{g}_\theta(p) = \mathrm{Re}\left(\frac{1}{N}\sum_{k=0}^{N-1}\widetilde{G}_{\theta,k}\exp\left(\frac{i2\pi kn}{N}\right)\right) \qquad n = 0, 1, ..., N-1 \tag{4}$$

Finally, back projection is used to convert this filtered projection vector into a 2D function. At a single angle, θ_m, the back projection is calculated as

$$f_{B,\theta_m}(x, y) = \widetilde{g}_{\theta_m}(x\cos\theta_m + y\sin\theta_m) \tag{5}$$

From this equation, and the fact that the value of p is the same for all (x, y) that lie on line L, it can be understood that the filtered projection makes the same contribution to the back projection at all points (x, y) that lie on L. In this way, the filtered projection is smeared back, or back projected, over the reconstructed image plane.

The accuracy of the reconstruction is dramatically improved through the use of projections at multiple angles. The reconstructed function is calculated as the sum of the back projections at each angle

$$f_{B,total}(x, y) = \sum_{m=0}^{M-1} f_{B,\theta_m}(x, y)\Delta\theta \tag{6}$$

where M is the number of projections, or angles, used in the reconstruction. For a complete reconstruction, angles between 0 and π are necessary, and therefore $\Delta\theta = \pi/M$. A visual illustration of this back projection method is given in a later section. This 2D filtered back projection method can be also used to reconstruct a 3D function $f(x, y, z)$ by reconstructing the function $f(x, y)$, as described above, for each value of z.

D. Reconstructed crescent geometry

In order to define the crescent geometry for modeling purposes, we more closely investigate the geometry of the TEM reconstruction. Based on the reconstruction, we choose the model crescent to consist of a 200 nm diameter dielectric core and a 270 nm diameter Au shell displaced by 32.5 nm. The gap in the tips is chosen to be 145 nm, resulting in tips with a radius of curvature of 5.5 nm. A side-by-side comparison of the central slice of the reconstruction to the central slice of the model is given in Figure S6. Visual inspection

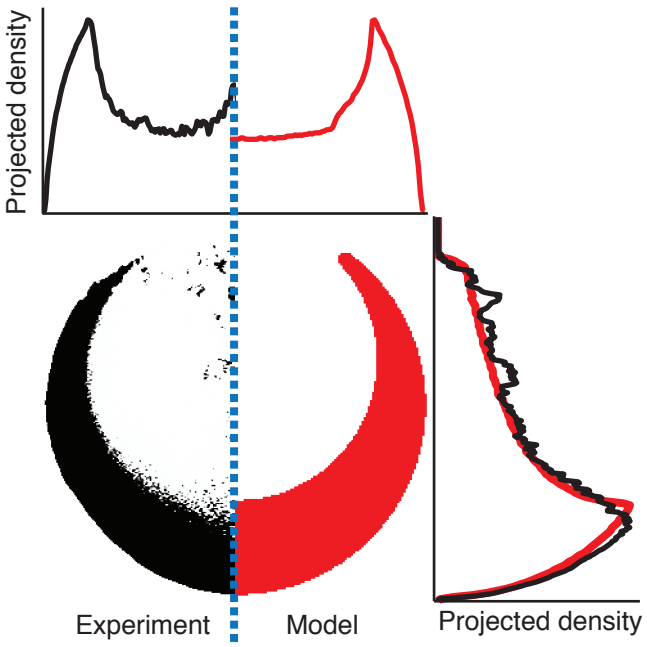

FIG. S6. **Reconstructed crescent geometry** Central slice of the TEM reconstruction (black) and the model used in FDTD (red). Projected densities along the vertical (top) and horizontal (right) directions show excellent agreement between the two geometries.

suggests that the simulated geometry (red) is quite similar to the TEM reconstruction (black), aside from the detailed geometry of the tips, which are sharper in the experiment.

To quantitatively compare the two geometries, we project the density of each along two orthogonal axes. The plot at the top of Figure S6 depicts the projection in the vertical direction, while the plot at the right of the figure depicts the projection in the horizontal direction. These projected densities illustrate the excellent agreement between the model geometry and the experimental TEM reconstruction.

E. Effect of substrate on crescent tilt-series

In order to construct a tilt-series of crescents for tomographic reconstruction, we must rely on distinct crescents with different orientations relative to the substrate. This is due to the inability to tilt the sample in the CL SEM. An important assumption of this multi-particle tomography method is that the properties under study are not significantly affected by the substrate. We justify this assumption by considering two important dipole locations,

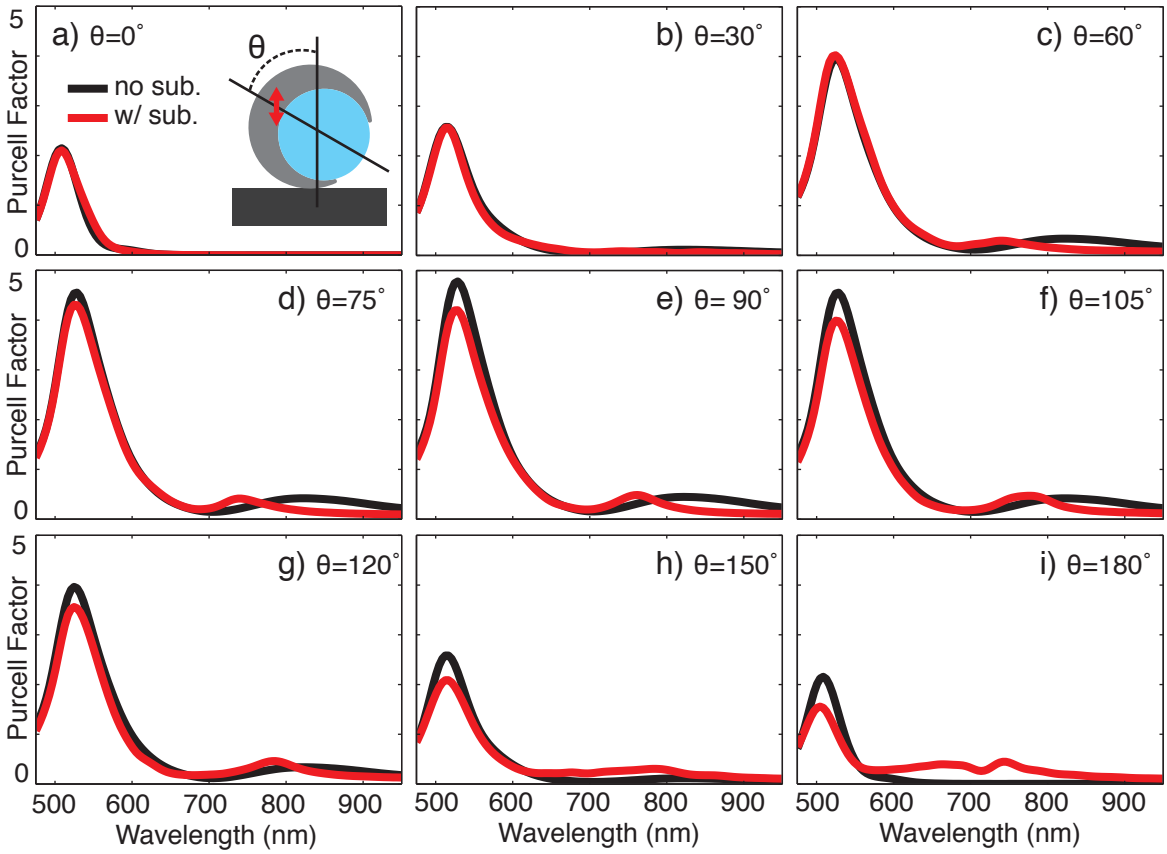

FIG. S7. **Substrate effects** The Purcell Factor (PF), or radiative rate enhancement, for a dipole located inside the metal base of the crescent. The angle between the crescent's axis of symmetry and the substrate normal is defined as θ, as shown in the schematic inset. a)-i) Data for angles of 0°, 30°, 60°, 75°, 90°, 105°, 120°, 150°, and 180° are shown. The PF with no substrate (black curves) are compared to the PF with substrate (refractive index n=3.7) at θ (red curves).

as shown in Figures S7 and S8.

The first dipole is located in the metal base of the crescent, 55 nm from the outer edge, as depicted in the schematic inset of Figure S7(a). This dipole location is chosen because of the importance of metal luminescence in the CL signal. The second dipole is located in the dielectric core of the crescent, 72.5 nm from the outer edge along the crescent's axis of symmetry, and oriented perpendicular to the substrate (refractive index = 3.7), as depicted in the schematic inset of Figure S8(a). This dipole location is chosen for its ability to excite both the low energy gap mode at the tips of the crescent, as well as higher energy modes. The angle between the crescent's axis of symmetry and the substrate normal is defined as θ.

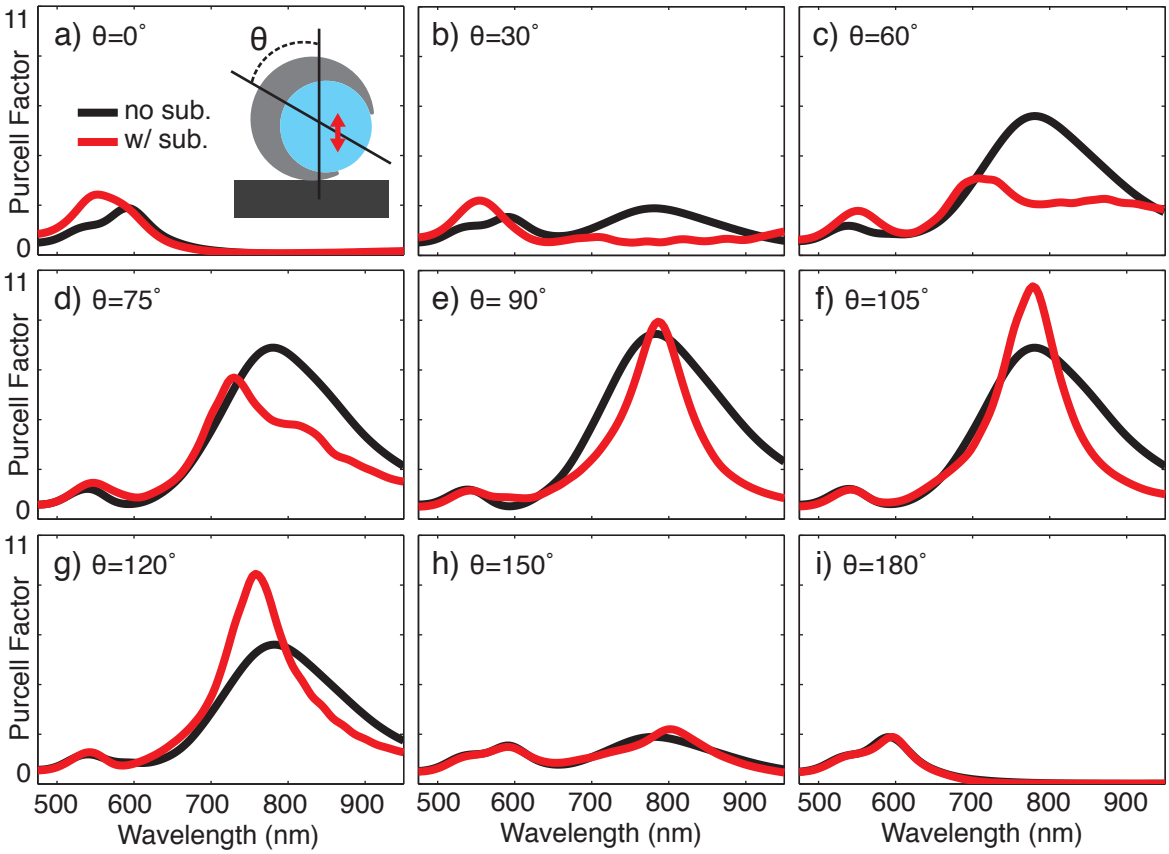

FIG. S8. **Substrate effects** The Purcell Factor (PF), or radiative rate enhancement, for a dipole located inside the crescent's dielectric core. The angle between the crescent's axis of symmetry and the substrate normal is defined as θ, as shown in the schematic inset. a)-i) Data for angles of 0°, 30°, 60°, 75°, 90°, 105°, 120°, 150°, and 180° are shown. The PF with no substrate (black curves) are compared to the PF with substrate (refractive index n=3.7) at θ (red curves).

Note that in the absence of particle-substrate interactions, angles of θ and $180° - \theta$ would give the same response.

Figures S7(a)-(i) and S8(a)-(i) (red curves) plot the Purcell Factor, or radiative rate enhancement, spectra for angles of 0°, 30°, 60°, 75°, 90°, 105°, 120°, 150°, and 180°, respectively. The black curves represent the PF when no substrate is present. Figure S7 demonstrates that the substrate has a negligible effect on the LDOS within the base of the metal shell of the crescent. From Figure S8, it can be seen that the substrate diminishes the intensity of the peak near 800 nm for angles close to 0°. However, for angles of 75° and above, the effect of the substrate is minimal, as the spectra with and without substrate agree

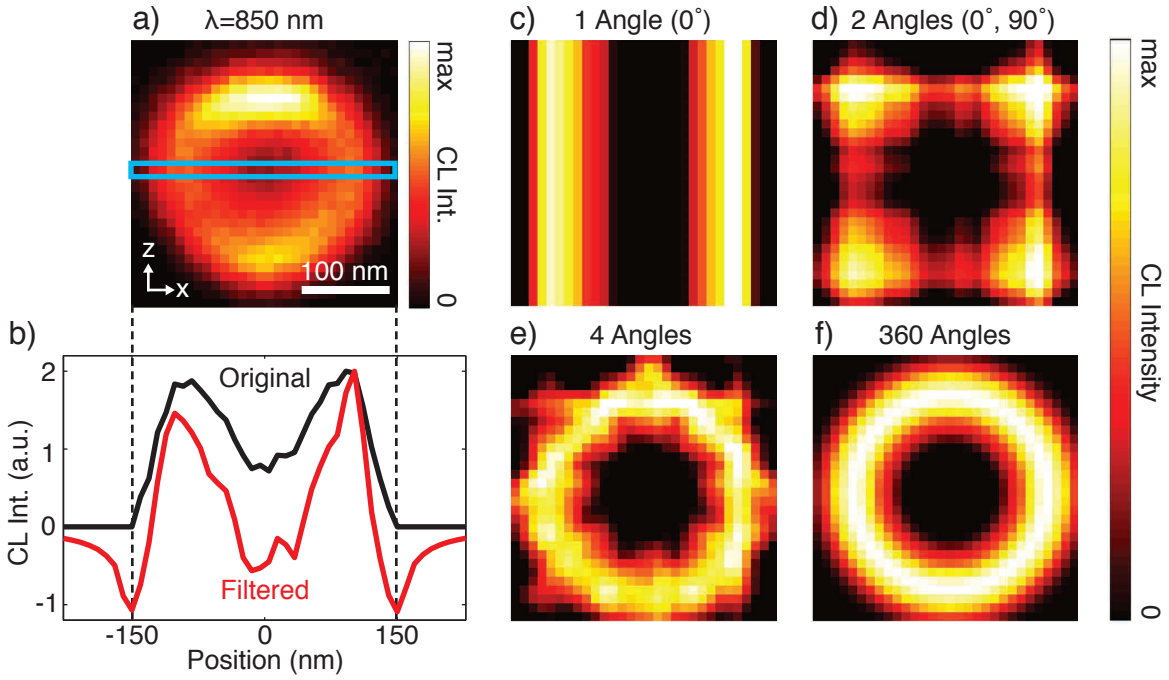

FIG. S9. **CL reconstruction method** a) 2D CL map at 850 nm of the crescent at 90°. The blue box encloses the z height used in the reconstruction. b) CL line scan before (black) and after (red) filtering in the frequency domain. c)-f) Reconstructions in the (x, y) plane made with the method of back projection using 1, 2, 4, and 360 angles, respectively.

well. For these reasons, we perform the multi-crescent tomographic reconstruction using a tilt-series composed of crescents at angles of 75° and above.

F. Step-by-step CL reconstruction

To elucidate the reconstruction of the CL signal by the method of filtered back projection, we illustrate the step-by-step process in Figure S9. For simplicity, we explain the reconstruction based on a single CL image, but the method is general and is used for the reconstruction based on the full tilt-series, as well. Figure S9(a) shows the CL map at 850 nm for the crescent oriented at 90°, with its axis of rotational symmetry perpendicular to the incident electron beam. Assuming the crescent is rotationally symmetric and ignoring any substrate effects, we can use this CL map as a virtual tilt-series spanning the full 360° of rotation.

As mentioned before, the 3D reconstruction is accomplished by carrying out a 2D recon-

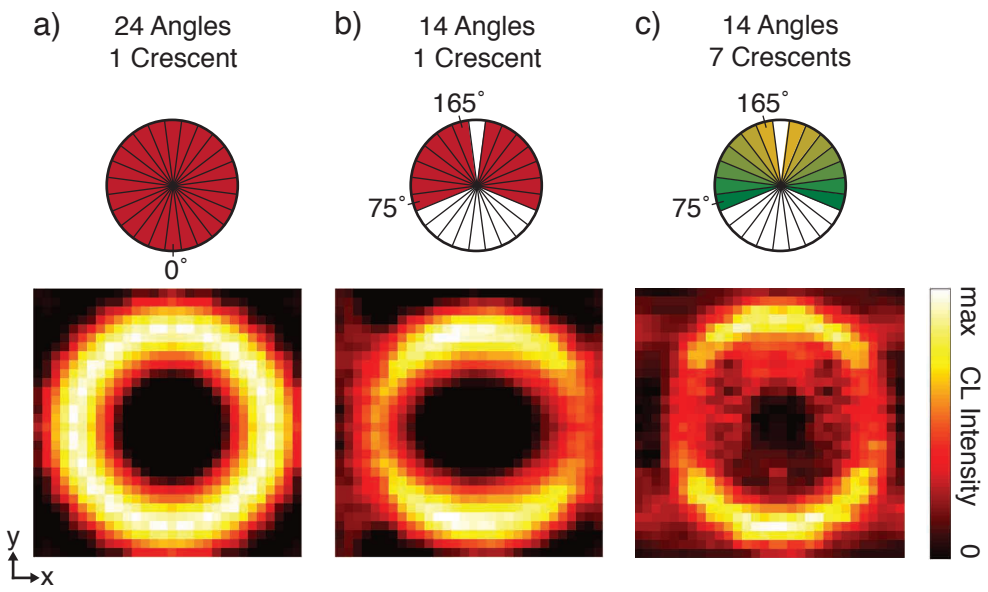

FIG. S10. **Effect of missing wedge** Reconstructions of CL at 850 nm at the midpoint in z, as described in Figure S9. a) Reconstruction in the (x, y) plane based on a single CL map used for angles between 0° and 360° in 15° increments. b) Reconstruction in the (x, y) plane based on a single CL map used for a limited tilt-series, with angles from 75° to 165° and 195° to 285° in 15° increments. c) Reconstruction in the (x, z) plane based on CL maps of seven different crescents with angles between 75° and 165° in 15° increments. Taking into account reflection symmetry, these crescents are also used for angles between 195° and 285°.

struction in the (x, y) plane at each value of z. For this example, an intermediate value of z is chosen, as highlighted by the blue box in Figure S9(a). This data is a CL line scan through the crescent, perpendicular to its axis of symmetry, as shown by the black curve in Figure S9(b), where data points beyond the boundaries of the scan have been set to zero. The red curve in this plot is the CL signal after being filtered in the frequency domain by a ramp filter multiplied by a Hann window, as given in Equation (3).

To illustrate the back projection method, reconstructions using an increasing number of angles are given in Figures S9(c)-(f). When only a single angle, 0°, is used for the reconstruction (Figure S9(c)), it can be seen that the filtered function is simply smeared across the reconstructed image plane in the vertical direction. When two angles, 0° and 90°, are used (Figure S9(d)), the vertical and horizontal back projections sum to give a square-like pattern. With the four angles 0°, 45°, 90° and 135° (Figure S9(e)), the donut-like form

begins to take shape. Figure S9(f) shows the complete reconstruction using 360 angles, or a projection every degree. From these figures it is clear that the accuracy of the reconstruction is dramatically improved through the use of projections at multiple angles. However, it is also important to note that even with only 4 angles, the general shape of the reconstructed function is apparent. This indicates that the tomogram based on the actual tilt-series data, which makes use of 14 angles, should, in fact, capture the essence of the 3D CL signal.

It is important to note that, due to experimental restrictions, a complete 360° tilt-series was not acquired. Instead, a limited range of angles is used for the reconstruction based on multiple crescents. Figure S10 illustrates the effect of using a limited tilt-series by comparing reconstructions of the CL at 850 nm at the midpoint in z, as described in Figure S9. Figures S10(a) and (b) show reconstructions in the (x, y) plane based on the single CL map for the crescent at 90°. For Figure S10(a), a complete 360° tilt-series (24 angles, in 15° increments) is created by making use of the rotational symmetry of the crescent, resulting in a radially symmetric reconstruction. In contrast, Figure S10(b) is created from a limited tilt series, consisting of the fourteen angles spanning 75° to 165° and 195° to 285°. These angles are chosen because they are the angles used for the multi-crescent tilt series. The reconstructions in Figures S10(a) and (b) agree quite well. However, the reconstruction based on the limited tilt series shows slight skewing in the x direction, due to the missing wedge of information. This same skew effect is seen in Figure 4(c) of the main text. For the sake of comparison, Figure S10(c) shows the result of the multi-crescent reconstruction, carried out in the (x, z) plane, and based on 7 different crescents. Note that the missing wedge results in the skewing in the x direction in this image, but is not responsible for the intensity variations in the radial direction. Those variations accurately reflect the experimental data, and arise from performing the reconstruction at different values of y.

G. CL tilt-series reconstruction

As described in the text, while the rotational symmetry of the crescent allows for a simple reconstruction of the CL signal from a single CL map, this symmetry is not a requirement of the CL tomography method. We also reconstruct the CL signal with the CL maps of crescents at different orientations. For this tilt-series, we consider crescents with angles between 75° and 165°, in 15° increments, ignoring angles between 0° and 60° for the reasons

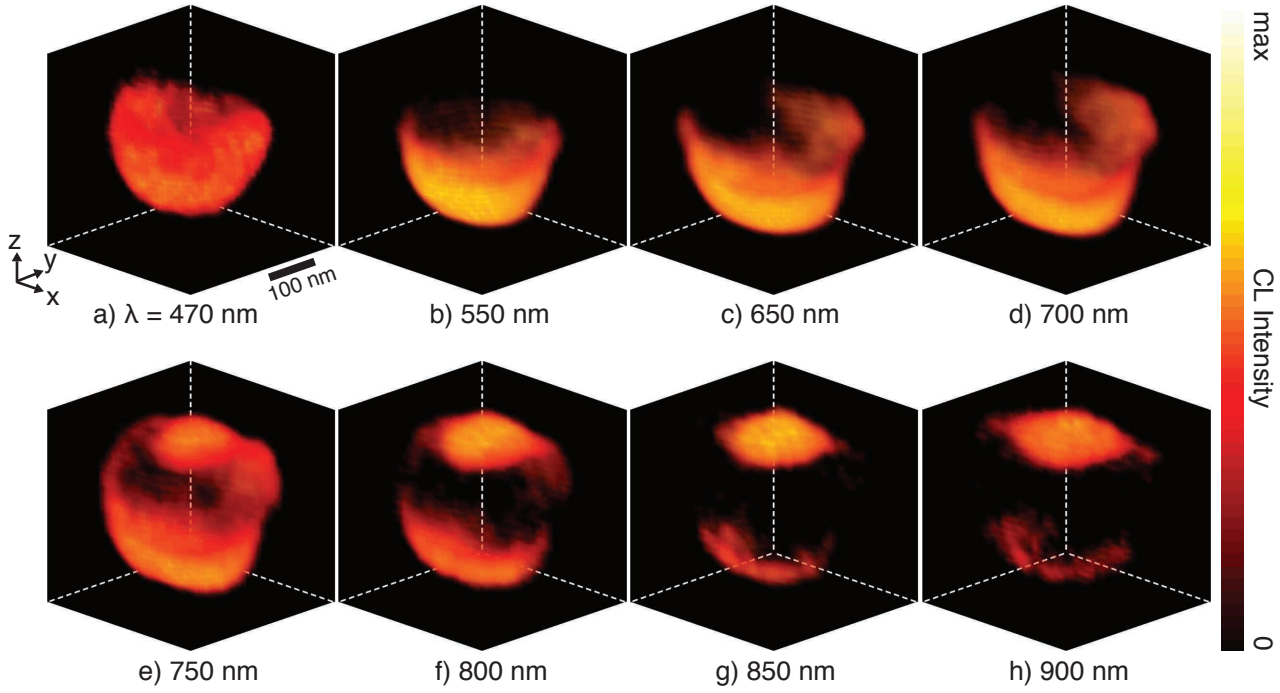

FIG. S11. **3D CL Spectroscopic Tomography** Reconstructed CL signal based on experimental tilt-series (reconstruction in (x, z) planes) at wavelengths of a) 470 nm, b) 550 nm, c) 650 nm, d) 700 nm, e) 750 nm, f) 800 nm, g) 850 nm, and h) 900 nm. The reconstructed intensity corresponds to both the color scale and the transparency of the figure.

stated above. Due to the reflection symmetry of the crescent, crescents at angles between 75° and 165° are equivalent to those at angles between 195° to 285°, and thus the tilt series is composed of 14 different angles.

Figure S11 shows the 3D CL tomograms at wavelengths between 470 nm and 950 nm. In these figures, the intensity of the reconstructed function corresponds to both the color scale and the transparency of the figure. These CL tomograms agree remarkably well with the CL tomograms shown in the main text, generated from the single crescent virtual tilt series. Most importantly, for shorter wavelengths we see that the CL signal is concentrated primarily in the metallic shell of the crescent, as expected for radiation from the Au. At longer wavelengths, efficient excitation of the gap mode can be seen clearly towards the top of the tomograms, near the tips of the crescent, as predicted by theory.

REFERENCES

[1]A. Mooradian, "Photoluminescence of metals," Physical Review Letters, **22**, 185 (1969).

[2]F. J. García de Abajo, "Optical excitations in electron microscopy," Reviews of Modern Physics, **82**, 209 (2010).

[3]X. Wu, T. Ming, X. Wang, P. Wang, J. Wang, and J. Chen, "High-photoluminescence-yield gold nanocubes: for cell imaging and photothermal therapy," ACS nano, **4**, 113 (2009).

[4]M. Yorulmaz, S. Khatua, P. Zijlstra, A. Gaiduk, and M. Orrit, "Luminescence Quantum Yield of Single Gold Nanorods," Nano Letters, **12**, 4385 (2012).

[5]M. B. Mohamed, V. Volkov, S. Link, and M. A. El-Sayed, "The lightning gold nanorods: fluorescence enhancement of over a million compared to the gold metal," Chemical Physics Letters, **317**, 517 (2000).

[6]M. R. Beversluis, A. Bouhelier, and L. Novotny, "Continuum generation from single gold nanostructures through near-field mediated intraband transitions," Physical Review B, **68**, 115433 (2003).

[7]E. Dulkeith, T. Niedereichholz, T. Klar, J. Feldmann, G. von Plessen, D. Gittins, K. Mayya, and F. Caruso, "Plasmon emission in photoexcited gold nanoparticles," Physical Review B, **70**, 205424 (2004).

[8]H. Hu, H. Duan, J. K. W. Yang, and Z. X. Shen, "Plasmon-Modulated Photoluminescence of Individual Gold Nanostructures," ACS nano, **6**, 10147 (2012).

[9]D. Cai, A. Neyer, R. Kuckuk, and H. M. Heise, "Raman, mid-infrared, near-infrared and ultraviolet–visible spectroscopy of PDMS silicone rubber for characterization of polymer optical waveguide materials," Journal of Molecular Structure, **976**, 274 (2010).

[10]G. A. George, "The phosphorescence spectrum and photodegradation of polystyrene films," Journal of Applied Polymer Science, **18**, 419 (1974).

[11]X. Y. Wang, R. Lockwood, M. Malac, H. Furukawa, P. Li, and A. Meldrum, "Reconstruction and visualization of nanoparticle composites by transmission electron tomography," Ultramicroscopy, **113**, 96 (2012).

[12]M. Lyra and A. Ploussi, "Filtering in SPECT Image Reconstruction," International Journal of Biomedical Imaging, **2011**, 1 (2011).

[13]I. Arslan, J. R. Tong, and P. A. Midgley, "Reducing the missing wedge: High-resolution

dual axis tomography of inorganic materials," Ultramicroscopy, **106**, 994 (2006).